# Effect of cohesion on shear banding in quasi-static granular material

Abhinendra Singh,* Vanessa Magnanimo, Kuniyasu Saitoh, and Stefan Luding
*Multi Scale Mechanics (MSM), Faculty of Engineering Technology, MESA+,*
*University of Twente, P.O. Box 217, 7500 AE Enschede, The Netherlands.*
(Dated: May 7, 2014)

Very often when dealing with powder technology, a fundamental point is raised, what is the effect of contact cohesion on the bulk behavior? A dimensionless parameter to determine the intensity of cohesive forces is the *granular Bond number* (*Bo*). Using DEM simulations, we investigate the effect of contact cohesion on slowly sheared dense, dry, frictional-cohesive powders in a split bottom Couette cell. Because of the geometry a wide stable shear band forms and the steady state becomes the focus. The shear banding phenomenon is independent of cohesion for Bond number $Bo < 1$ and dependent on cohesion for $Bo \geq 1$, when cohesive forces start to play an important role. Inside the shear band, we find that the mean normal contact force is independent of cohesion, while the forces carried by contacts along the (compressive and tensile) eigen-directions of the local strain rate are cohesion dependent. Forces carried by contacts along the compressive and tensile directions are symmetric about the mean force, while the force along the neutral direction is like the mean total force. The anisotropy of the force network increases with cohesion. Cohesion also increases the heterogeneous structures in both compressive and tensile directions.

## I. INTRODUCTION

Granular materials such as sand and limestone, neither behave like elastic solids nor like normal fluids, which makes their motion difficult to predict. When they yield under slow shear, the relative motion is confined to narrow regions (between large solid-like parts) called shear bands [1–3]. Shear bands are observed in many complex materials, which range from foams [4] and emulsions [5, 6] to colloids [7] and granular matter [1, 2, 8–17]. There has been tremendous effort to understand the shear banding in flow of non-cohesive grains [1, 2, 8–19]. However, real granular materials often experience inter-particle attractive forces due to many physical phenomena: *van der* Waals force due to atomic forces for small grains [20–22], *capillary* forces due to presence of humidity [23], *solid bridges* [24, 25], coagulation of particles [26], and many more.

The question, arises how does the presence of attractive forces affect shear banding? So far, only a few attempts have been made to answer this question, concerning dense metallic glasses [27, 28], adhesive emulsions [29, 30], attractive colloids [31–33], cemented granular media [34], wet granular media [35, 36] and clayey soils [37]. Recently, rheological studies on adhesive emulsions and colloids [29–31, 33] reported that the presence of attractive forces at contact affects shear banding by affecting flow heterogeneity and wall slip.

Another unique yet not completely understood feature of granular materials is their highly heterogeneous contact force distribution. The heterogeneity in the force distribution has been observed in both experimental and numerical studies [2, 38–46]. While huge effort has been made to understand the force distribution of non-cohesive particles [2, 38–44, 47], only limited studies have aimed to understand the same for assemblies with attractive interactions [21, 48–52]. Richefeu et al. [49] studied the stress transmission in wet granular system subjected to isotropic compression. Gilabert et al. [50] focussed on a two-dimensional packing made of particles with short-range interactions (cohesive powders) under weak compaction. Yang et al. [51] studied the effect of cohesion on force structures in a static granular packing by changing the particle size. In a previous study [53], the effect of dry cohesion at contact on the critical state yield stress was studied. The critical-state yield stress shows a peculiar non-linear dependence on the confining pressure related to cohesion. But the microscopic origin was not studied.

In this paper, we report the effect of varying attractive forces at contact on the steady state flow behavior and the force structure in sheared dry cohesive powders. Discrete Element Method (DEM) simulations are used to investigate the system at micro (partial) and macro level. In order to quantify the intensity of cohesion, a variation of the *granular Bond number* [50, 54, 55] is introduced. We find that this dimensionless number very well captures the transition from a gravity/shear-dominated regime to the cohesion-dominated regime. To understand this further we look at the effect of cohesion on the mean force and anisotropy, by investigating the forces along the eigen-directions of the local strain rate tensor. Intuitively, one would expect only the tensile direction to be affected by cohesion, but the real behavior is more complex. We also discuss the probability distributions and heterogeneities of the forces in different directions to complete the picture.

The paper is organized in four main parts. Section II describes the model system in detail specifying the geometry, details of particle properties, interaction laws. In section III, the velocity profiles and shear band from samples with different contact cohesion are presented. In the same section, the force anisotropy and probabilities are studied too. Finally, section IV is dedicated to the discussion of the results, conclusions and an outlook.

*a.singh-1@utwente.nl

## II. DISCRETE ELEMENT METHOD SIMULATION (DEM)

In this section, we explain our DEM simulations. We introduce a model of cohesive grains in Sec. II A and show our numerical setup in Sec. II B. In Sec. II C, we introduce a control parameter, i.e. *global Bond number*, which governs the flow profiles and structure of the system.

### A. Model

Discrete Element Methods (DEM), provide numerical solutions of Newton's equations of motion based on the specification of particle properties viz. stiffness, density, radius and a certain type of interaction laws like Hertzian/Hookean [56, 57]. Simulation methodology and material parameters used in this study are the same as in our previous work [53, 58]. The adhesive elasto-plastic contact model [59] is used to simulate cohesive bulk flow, is briefly explained below.

For fine, dry powders, adhesive properties due to van der Waals forces and plasticity and irreversible deformation in the vicinity of the contact have to be considered at the same time [60, 61]. This complex behavior is modeled using a piecewise linear hysteretic spring model [59]. Few other contact models in similar spirit are also recently proposed [62, 63].

The adhesive, plastic (hysteretic) force is introduced by allowing the normal unloading stiffness to depend on the history of deformation. During initial loading the force increases linearly with overlap $\delta$ along $k_1$, until the maximum overlap $\delta_{\max}$ is reached, which acts as a history parameter. During unloading the force decreases along $k_2$, the value of which depends on the maximum overlap $\delta_{\max}$ as given by Eq. (2). The overlap when the unloading force reaches zero, $\delta_0 = (1-k_1/k_2)\delta_{\max}$, resembles the permanent plastic deformation and depends nonlinearly on the previous maximal force $f_{\max} = k_1\delta_{\max}$. The negative forces reached by further unloading are attractive, cohesion forces, which also increase nonlinearly with the previous maximum force experienced. The maximal cohesion force that corresponds to the "pull–off"force, is given by

$$f_{\mathrm{m}} = -k_c\delta_{\min}, \tag{1}$$

with $\delta_{\min} = \frac{k_2-k_1}{k_2+k_c}\delta_{\max}$.

Three physical phenomena: elasticity, plasticity and cohesion are quantified by three material parameters $k_p$, $k_1$, and $k_c$, respectively. Plasticity disappears for $k_1 = k_p$ and cohesion vanishes for $k_c = 0$.

In order to account for realistic load-dependent contact behavior, the $k_2$ value is chosen to depend on the maximum overlap $\delta_{\max}$, i.e. *particles are more stiff for larger previous deformation* and the so dissipation is dependent on deformation. The dependence of $k_2$ on overlap $\delta_{\max}$ is chosen empirically as linear interpolation

$$k_2(\delta_{\max}) = \begin{cases} k_p & \text{if } \delta_{\max}/\delta^p_{\max} \geq 1 \\ k_1 + (k_p - k_1)\frac{\delta_{\max}}{\delta^p_{\max}} & \\ & \text{if } \delta_{\max}/\delta^p_{\max} < 1 \end{cases} \tag{2}$$

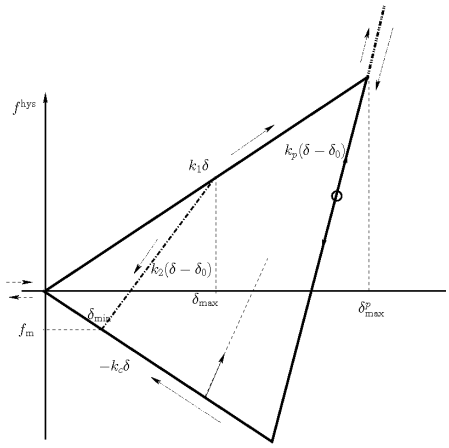


FIG. 1: Schematic graph of the piece-wise linear, hysteretic, and adhesive force-displacement model in normal direction.

As discussed in Ref. [59], very large deformations will lead to a quantitatively different contact behavior, a maximal force overlap $\delta^p_{\max} = \frac{k_p}{k_p-k_1}\frac{2a_1a_2}{a_1+a_2}\phi_f$ is defined (with $\phi_f = 0.05$). Above this overlap $k_2$ does not increase anymore and is set to the maximal value $k_2 = k_p$. This visco-elastic, reversible branch is referred to as "limit branch" and is discussed in detail in [59].

The contact friction is set to $\mu = 0.01$, i.e. artificially small, in order to be able to focus on the effect of contact cohesion only. In order to study the influence of contact cohesion, we analyzed the system for the following set of adhesivity parameters $k_c$:

$$k_c \in [0,5,10,25,33,50,75,100,200]\,\mathrm{Nm}^{-1}\,, \tag{3}$$

which has to be seen in relation to $k_1 = 100$ Nm$^{-1}$. Other parameters, such as the jump–in force $f_a$ [58] and $\phi_f$ [58, 59] are not varied here.

### B. Split-bottom ring shear cell

Figure 2 is a sketch of our numerical setup (the geometry of the system is described in detail in Refs. [15, 64–67]). In this figure, the inner, split, and outer radii are given by $R_i$, $R_s$, and $R_o$, respectively, where the concentric cylinders rotate relative to each other around the symmetry axis (the dot-dashed line). The ring shaped split at the bottom separates the moving and static parts of the system, where a part of the bottom and the outer cylinder rotate at the same rate. The system is filled with $N \approx 3.7\times10^4$ spherical particles with density $\rho = 2000\,\mathrm{kg/m^3} = 2\,\mathrm{g/cm^3}$ up to height $H$. The average size of particles is $a_0 = 1.1\,\mathrm{mm}$, and the width of

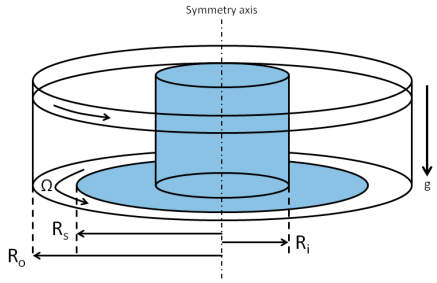


FIG. 2: (Color online) A sketch of our numerical setup consisting of a fixed inner part (light blue shade) and a rotating outer part (white). The white part of the base and the outer cylinder rotate with the same angular velocity $\Omega$ around the symmetry axis. The inner, split, and outer radii are given by $R_i = 0.0147\,\mathrm{m}$, $R_s = 0.085\,\mathrm{m}$, and $R_o = 0.11\,\mathrm{m}$, respectively, where each radius is measured from the symmetry axis. The gravity $g$ points downwards as shown by arrow.

the homogeneous size-distribution (with $a_{\min}/a_{\max} = 1/2$) is $1 - \mathscr{A} = 1 - \langle a \rangle^2/\langle a^2 \rangle = 0.18922$. The cylindrical walls and the bottom are roughened due to some (about 3% of the total number) attached/glued particles [65, 66].

When there is a relative motion at the split, a shear band propagates from the split position $R_s$ upwards and inwards, remaining far away from cylinder-walls and bottom in most cases. The qualitative behavior is governed by the ratio $H/R_s$ and three different regimes can be identified, as reported in Refs. [67–70]. We keep $H/R_s < 0.5$, such that the shear band reaches the free surface and stays away from inner wall [68, 69].

Translational invariance is assumed in the tangential $\phi-$direction, and the averaging is performed over toroidal volumes, over many snapshots in time. This leads to fields $Q(r,z)$ as function of the radial and vertical positions. The averaging procedure has been explained in detail for three dimensional systems in [53, 65, 66], and is not further discussed here.

Since we are interested in the quasi-static regime, the rotation rate of outer cylinder is chosen to be $0.01\,\mathrm{s}^{-1}$, such that the inertial number $I = \frac{\dot{\gamma} d}{\sqrt{p/\rho}}$ [71] is $I \ll 1$. The simulation runs for more than 50 s.

### C. Bond number

Intensity of cohesion can be quantified by a ratio of the maximum attractive force to a typical force scale in the system. For example, Nase et al. [54] introduced the granular Bond number under gravity, which compares the maximum attractive force at contact with the weight of a single grain. For plane shear without gravity, other authors [50, 55] used a ratio between the maximum attractive force and the average force due to the confining pressure. In our analysis, we introduce a *global Bond number* as

$$Bo = \frac{f_{\mathrm{m}}}{\langle f \rangle}\,, \tag{4}$$

where $f_{\mathrm{m}}$ and $\langle f \rangle$ are the maximum allowed attractive force reached at a contact (given by the contact model, Eq. (1)) and the mean force per contact reached close to the bottom, respectively. For the calculation of mean force $\langle f \rangle$, layer of two particles diameters which is few particle diameter away from bottom is chosen. Because the shear band initiates from the bottom, we choose the mean force $\langle f \rangle$ at the bottom to understand the effect of cohesion on these shear bands.

It is important to mention that the mean compressive force (at the bottom) corresponds to the weight of the material above, whereas the maximum attractive force corresponds to the pull-off force, which is directly related to the surface energy of the particles. These two material and particle properties are easily accessible experimentally.

The Bond number is a measure of the importance of adhesive forces compared to compressive forces. A low Bond number indicates that the system is relatively unaffected by attractive force effects; a high number (typically larger than one) indicates that attractive forces dominate. Intermediate numbers indicate a non-trivial balance between the two effects.

In parallel with the global Bond number as defined above, we also define two local variants of this quantity. A local simulation based Bond number $Bo_l^s(P) = f_{\mathrm{m}}^s(P)/\langle f(P) \rangle$ can be define by comparing the maximum attractive force reached at a given pressure (which can be less than or equal to the maximum allowed attractive force given by the contact model) with the mean force at that pressure (subscript $l$ represents the local quantity, while superscript $s$ denotes that this definition takes input from simulation data). Another variant of this $Bo_l^a(P)$ is defined in the Appendix, which compares the analytical prediction for the maximum attractive force with mean force at that pressure.

Figure 3 displays the global Bond number $Bo$ and the mean values of $Bo_l^s(P)$ and $Bo_l^a(P)$ (averaged over different pressure) as functions of the adhesivity parameter $k_c$, where the figure shows that local and global quantities are comparable with slight divergence for high cohesion $k_c$. For the sake of simplicity in the rest of this paper, we use the global Bond number $Bo$ to quantify the intensity of cohesion.

## III. RESULTS

In this section, we present our results of DEM simulations. In Sec. III A, we analyze the flow profiles and shear banding in our system. In Sec. III B, we study distributions and structures of force chain networks in shear bands. In Sec. III C, we explain anisotropic features of the force chain networks.

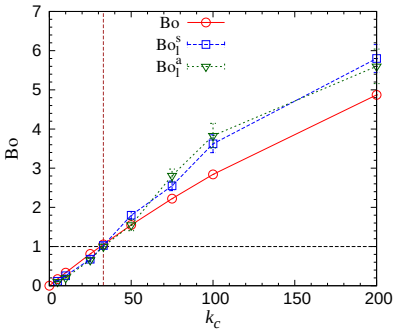


FIG. 3: (Color online) Variants of granular Bond number plotted against cohesive strength $k_c$, where the red circles represent the global Bond number $Bo$, while the blue squares and green triangles represent the average values of $Bo_l^s(P)$ and $Bo_l^a(P)$, respectively.

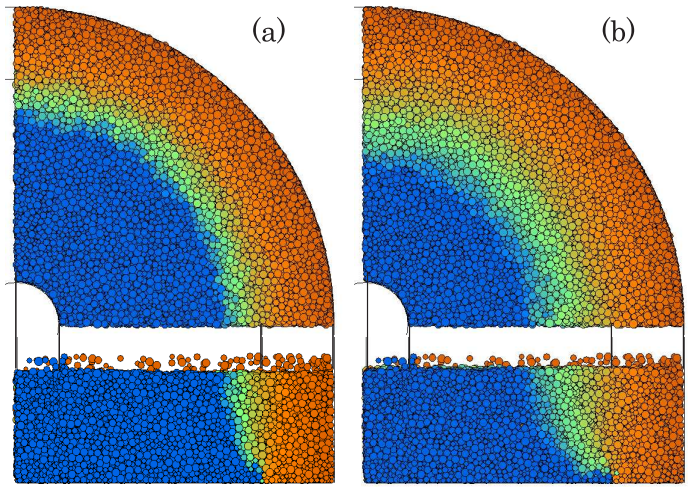


FIG. 4: (Color online) Snapshots from simulations with different cohesion strengths, but the same number of mobile particles $N = 34518$, seen from the top (Top) and from the front (Bottom). The material is (a) without cohesion $Bo = 0$, and (b) with strong cohesion $Bo = 4.86$. The colors blue, green, and orange denote the particles with displacements in tangential direction per second $r\,\mathrm{d}\phi \leq 0.5\,\mathrm{mm}$, $r\,\mathrm{d}\phi \leq 2\,\mathrm{mm}$, $r\,\mathrm{d}\phi \leq 4\,\mathrm{mm}$, and $r\,\mathrm{d}\phi > 4\,\mathrm{mm}$, respectively

### A. Effect of cohesion on Flow Profiles

Figure 4 displays both top- and front-view of samples with the same filling height, i.e. the same number of particles, and different global Bond numbers, $Bo =$ (left) 0 and (right) 4.86, respectively, where the color code represents the azimuthal displacement rate of the particles. From the front-view, the shear band (green colored area) moves inwards and gets wider with increasing "height", while the shear band also moves inwards and becomes wider with increasing "Bond number".

Figure 5 shows the non-dimensional angular velocity profiles at the top surface against radial coordinate normalized with mean particle diameter $\langle d \rangle$, where we assume translational invariance in the azimuthal direction and take averages over the toroidal volumes as well as many snapshots in time [13]. The angular velocity profile can be well approximated by an error function

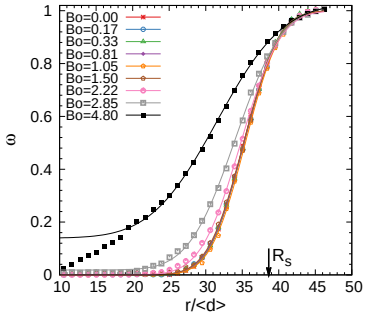


FIG. 5: (Color online) Non-dimensional angular velocity profile $\omega$ at the top surface plotted against the radial coordinate $r$ scaled by the mean diameter $\langle d \rangle$. Different symbols represent different values of the global Bond number given in the inset, where the solid lines represent the corresponding fits to Eq. (5).

$$\omega = A_1 + A_2 \mathrm{erf}\left(\frac{r - R_c}{W}\right) \tag{5}$$

as in the case of non-cohesive materials [15, 64–67], where $R_c$ and $W$ are the position and width of the shear band, respectively. Here, we use the dimensionless amplitudes, $A_1 = A_2 \approx 0.5$, for the whole range of the Bond numbers, while we use $A_1 = 0.6$ and $A_2 = 0.4$ for the strong cohesion with $Bo = 4.86$. The dimensionless amplitudes, $A_1$ and $A_2$ (along with estimated errors), are summarized in Table I. Figure 6 shows the position of the shear band relative to the split at bottom $R_s - R_c$ and the width of shear band $W$ (both scaled by mean particle diameter) at the top surface against the Bond number. Here, within the error-bars, both the position and width are independent of cohesion if $Bo < 1$. However, the shear band moves inside and becomes wider with the Bond number if $Bo > 1$.

Both the position and width of shear band also depend on the height ($z$) in the system. Figure 7 displays the non-dimensional position and width of the shear band for different values of $Bo$ as functions of the height scaled by the filling height, i.e. $z/H$. In this figure, the shear band moves closer to the inner cylinder and gets wider while approaching to the top layer, which is consistent with previous cohesive and non-cohesive studies [15, 53, 64–67, 70]. In Fig. 7(a), the lines are the prediction by Unger et al. [68]:

$$z = H - R_c \left\{ 1 - \frac{R_s}{R_c} \left[ 1 - \left( \frac{H}{R_s} \right)^{\beta} \right] \right\}^{1/\beta}, \tag{6}$$

where the exponent is given by $\beta = 2.5$ for non-cohesive particles. If the Bond number is less than one, our numerical data show very good agreement with Eq. (6). Above $Bo = 1$, however, the exponent $\beta$ decreases with the global Bond number

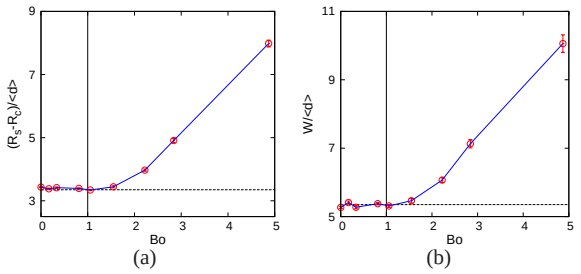


FIG. 6: (Color online) (a) Position and (b) width (both scaled by mean particle diameter) of shear band at the top surface plotted against the global Bond number. Symbols with error-bars are the data, while the lines are only a guide to eye.

as in Table I. Note that Eq. (6) slightly deviates from the results near the top surface if the cohesion is strong ($Bo = 2.22$ and 2.85). In Fig. 7(b), the lines are the prediction by Ries. et al. [70] for non-cohesive system:

$$W(z) = W_{\text{top}}\left[1 - \left(1 - \frac{z}{H}\right)^2\right]^{\gamma}, \qquad (7)$$

where $W_{\text{top}}$ is the width at the top surface and the exponent is given by $\gamma = 0.5$ for non-cohesive particles. If $Bo < 1$, Eq. (7) with $W_{\text{top}} = 0.012$ and $\gamma = 0.5 \pm 0.1$ well agrees with our results. However, for $Bo > 1$, both the width $W_{\text{top}}$ and exponent $\gamma$ increase with the global Bond number as in Table I. In addition, Eq. (7) deviates from the results near the top layer if the cohesion is strong ($Bo = 2.22$ and 2.85), where the width initially increases with the height, but saturates above $z/H \simeq 0.6$. Hence for $Bo > 1$, we choose width at that height to be $W_{\text{top}}$ and use $\gamma = 0.66$ and 0.7 for $Bo = 2.22$ and 2.85, respectively.

From the above results, we find that the cohesive forces between particles drastically affect the flow profiles. Eqs. (6) and (7) very well predict the position and width of the shear bands, respectively for $Bo < 1$. For large $Bo$ these equations do not work anymore at large heights since the shear band interferes with the inner cylinder. The shear band, which is the region with a large velocity gradient, is caused by *sliding motions* of particles. However, strong cohesive forces connect particles in contacts (in other words, the cohesive forces promote *collective motions* of particles) and prevent them from sliding. As a result, the velocity gradient is smoothened and the width of shear-band is broadened. This observation is consistent with previous studies on adhesive dense emulsions [72]. Interestingly, such an effect of cohesion is suppressed if the global Bond number is less than one, where our numerical data agrees well with previous theoretical/numerical studies on non-cohesive particles [68, 70]. Hence, we show that the global Bond number, $Bo$, captures the transition between essentially non-cohesive free-flowing granular assemblies ($Bo < 1$) to cohesive ones ($Bo > 1$).

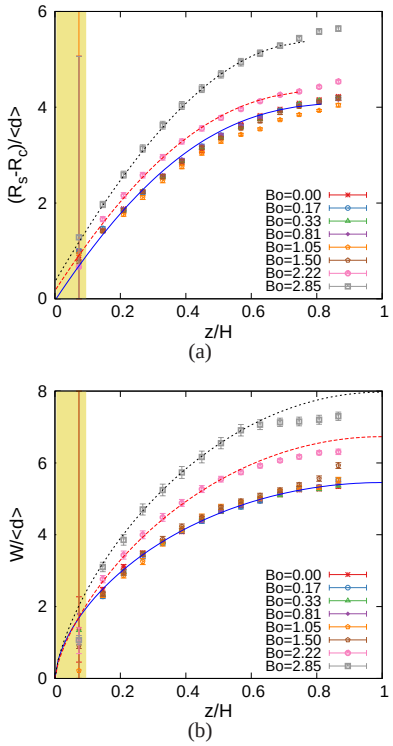


FIG. 7: (Color online) (a) Position and (b) width (both scaled by mean particle diameter) of shear band in the cell plotted against height $z$ scaled by the filling height $H$. Different symbols correspond to values of the global Bond number given in the inset. The lines in (a) and (b) are the predictions, Eqs. (6) and (7), respectively.

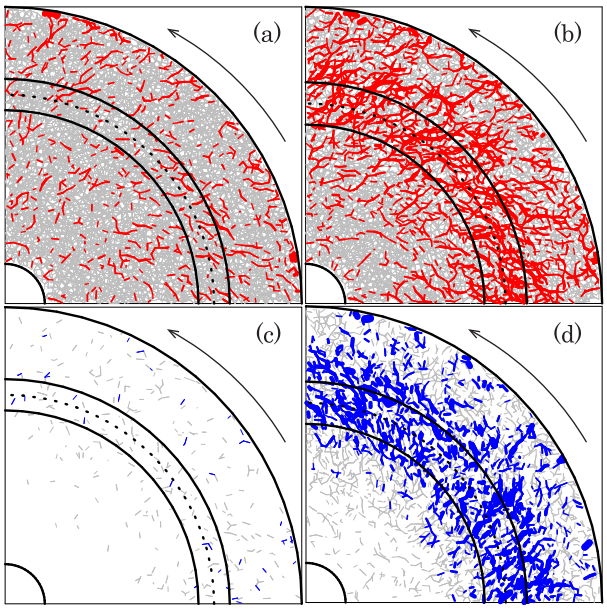


FIG. 8: (Color online) Force chain networks of positive normal forces for $Bo =$ (a) 0.33 and (b) 2.85, and negative normal forces for $Bo =$ (c) 0.33 and (d) 2.85 at height $0.02 < z < 0.05$ m, respectively.

| $Bo$ | $A_1$ | $A_2$ | $H$ | $\beta$ | $\frac{z}{H}$ range | $W_{\text{top}}$ | $\gamma$ |
|---|---|---|---|---|---|---|---|
| 0 | 0.50± 0.0005 | 0.500± 0.0005 | 0.0365 | 2.52 | 0.1-1 | 0.0117 | 0.507 |
| 0.17 | 0.50± 0.0005 | 0.499± 0.0005 | 0.0365 | 2.52 | 0.1-1 | 0.0118 | 0.523 |
| 0.33 | 0.49± 0.0007 | 0.500± 0.0007 | 0.0365 | 2.512 | 0.1-1 | 0.0118 | 0.555 |
| 0.81 | 0.49± 0.0008 | 0.500± 0.0008 | 0.0361 | 2.494 | 0.1-1 | 0.0119 | 0.583 |
| 1.05 | 0.49± 0.001 | 0.501± 0.001 | 0.0359 | 2.510 | 0.1-1 | 0.0120 | 0.582 |
| 1.50 | 0.49± 0.002 | 0.501± 0.002 | 0.0364 | 2.453 | 0.1-0.8 | 0.0126 | 0.613 |
| 2.22 | 0.49± 0.003 | 0.501± 0.003 | 0.0368 | 2.367 | 0.1-0.6 | 0.0138 | 0.667 |
| 2.85 | 0.49± 0.005 | 0.502± 0.005 | 0.0369 | 2.259 | 0.1-0.6 | 0.0160 | 0.713 |

TABLE I: Table showing filling height of the system $H$, and fitting range $z/H$ for Eqs. (6) and (7), together with the fit parameters $A_1$, $A_2$ in Eq. (5), $\beta$ in Eq. (6), $W_{top}$ and $\gamma$ in Eq. (7).

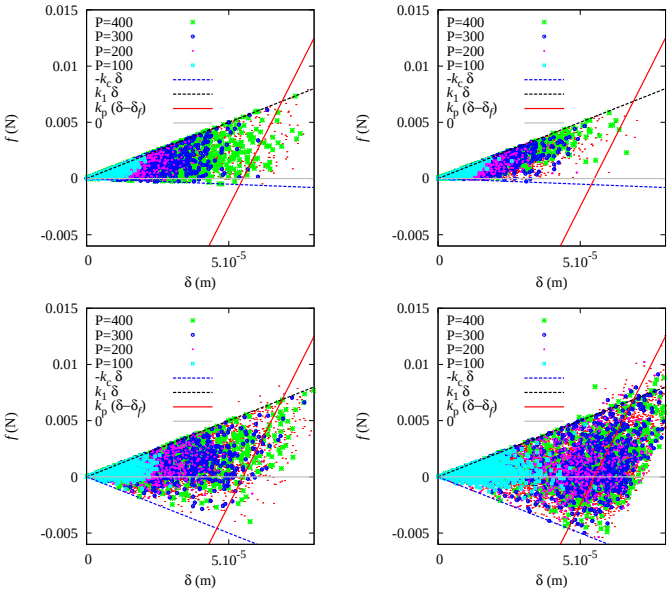


FIG. 9: (Color online) Scatter plots of overlaps and forces between all contacts inside (left) and outside (right) of the shear bands for different $Bo = 0.33$ and 2.85. The different symbols represent a zoom into the vertical ranges $z = 8$ mm ±1 mm (green stars), 15 mm ±1 mm (blue circles), 22 mm ±1 mm (magenta dots), 29 mm ±1 mm (cyan squares), with approximate pressure as given in the inset. Note that the points do not collapse on the line $k_p(\delta - \delta_f)$ due to the finite width of the size distribution: pairs of larger than average particles fall out of the indicated triangle. Radial range $0.075\,\text{m} \leq r \leq 0.085\,\text{m}$ (left) signifies data points inside the shear band, while the radial range $0.055\,\text{m} \leq r \leq 0.065\,\text{m}$ (right) signifies the data points outside the shear band.

### B. Structure and distribution of forces in shear bands

To understand the microscopic origin of the anomalous flow profiles of cohesive aggregates, we study the force network and statistics of the interparticle normal forces. Recently Wang et al. [73] reported the shape of probability distribution function (PDF) as an indicator for transition of flow from quasistatic to inertial flows. In this section, we use a similar philosophy to determine if there is any change in the shape of PDFs as the cohesive strength is increased.

Figure 8 shows force chains of positive ((a) and (b)) and negative ((c) and (d)) normal forces in the systems with low cohesion ((a) and (c)) and strong cohesion ((b) and (d)). Grey color shows the weak forces, while red and blue colors show the strong positive and negative forces respectively. The strong or weak positive forces are forces larger or smaller than the mean positive force $f_{\text{pos}}$. A similar approach is adopted to identify the strong/weak negative forces. In this figure, we observe that both positive and negative forces are fully developed in the cohesive system ((b) and (d)), where the intensity of the positive/negative force inside the shear band is stronger than outside. In addition, the strong (positive/negative) force chains are percolated through the shear band region. As explained in Sec. III C, we can also see that the positive and negative force chains are aligned in their preferred directions, i.e. compressive and tensile directions, respectively.

Figure 9 displays scatter plots of the interparticle forces against overlaps between the particles in contacts, where each point corresponds to a contact and different colors represent different height, i.e. pressure level in the system. The left and right columns are the results of inside and outside the shear bands, respectively. Higher the pressure $p$, higher is the average force (or overlap), to sustain a pressure due to the weight of the particles. For almost all values of $Bo$, the density of points towards unloading $k_p$ branch inside the shear band is higher compared to the points outside. We also observe that with increasing $Bo$, most contacts (except for small pressure) drift towards and collapse around the limit branch of the contact model (especially inside the shear band). This implies that *the cohesive forces are more pronounced in shear bands* rather than outside.

#### 1. *Mean force and overlap in shear bands*

Figure 10 displays the mean normal forces, $\langle f \rangle$, in the shear band plotted against pressure, $P$, for different values of the global Bond number, where the solid line is the prediction by Shaebani et al. [74] for non-cohesive granular systems as

$$\langle f \rangle = \frac{4\pi \langle a^2 \rangle}{\phi C g_2} \langle P \rangle \tag{8}$$

with the 2nd moment of the size distribution $\langle a^2 \rangle$, coordination number $C$, volume fraction $\phi$, and mean pressure $\langle P \rangle$.

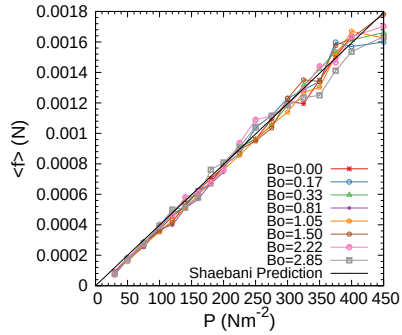


FIG. 10: (Color online) The mean normal force inside of the shear band plotted against pressure, where different symbols represent the global Bond number (as given in the inset) and the solid line is given by Eq. (8).

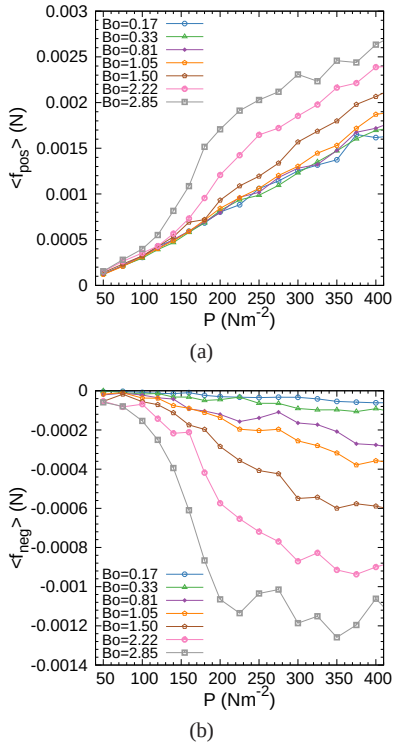


FIG. 11: (Color online) The mean (a) positive and (b) negative forces inside the shear band plotted against pressure, where different symbols represent the global Bond number (as given in the inset).

Notably, *the mean normal force is almost independent of cohesion* and linearly increases with pressure as in the cases of static non-cohesive [39, 45] and cohesive systems [51]. We also observe that for low pressure, Eq. (8) slightly over predicts the value of the mean force, while for higher pressure the prediction well captures the data. While the mean value is insensitive to cohesion, the mean positive and negative normal forces, $\langle f_{\rm pos}\rangle$ and $\langle f_{\rm neg}\rangle$, strongly depend on cohesion. Figure 11 shows the mean positive and negative forces against pressure for different values of *Bo*, where *the intensities increase*

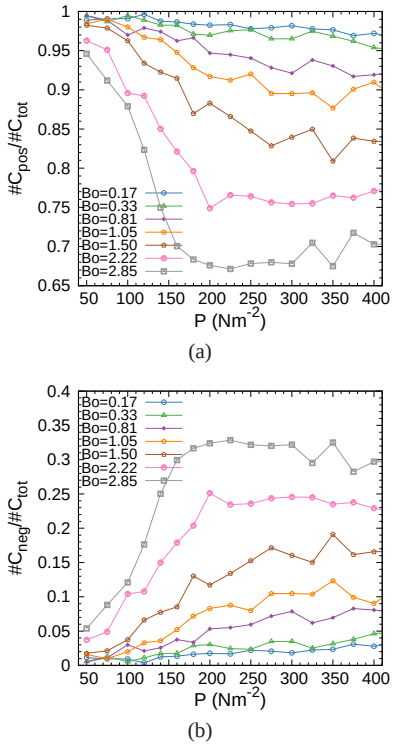


FIG. 12: (Color online) The fractions of (a) positive and (b) negative contacts inside the shear band plotted against pressure, where different symbols represent the global Bond number (as given in the inset).

*with cohesion* in agreement with Fig. 8. Note that the mean positive force is linear with pressure and independent of cohesion below $Bo = 1$, while its dependence on pressure becomes nonlinear above $Bo = 1$. Though the origin of this nonlinearity is not clear, it is readily understood that cohesion enhances the collective motion of the particles, i.e. the particles rearrange less and the system is in a mechanically constrained state. Because increasing cohesion increases the magnitude of negative forces, both the positive and negative force chains are strong to balance each other. It is noteworthy that in Fig. 9, the increase of *Bo* increases the density of points in both positive and negative extremes, inside the shear band.

The cohesive force seems not to affect the average number of contacts, see Ref. [58], where we reported that cohesion had practically no effect on the contact number density (volumetric fabric) in the same system. Fig. 12 shows the fractions of repulsive and attractive contacts against pressure for different Bond numbers, together with the overall coordination number. An increase of cohesion generates more attractive contacts while it decreases the number of repulsive contacts. Interestingly, the overall mean force remains independent of cohesion and contacts simply redistribute between the repulsive and attractive directions.

In contrast to the mean force, the mean overlap between particles in contact depends on cohesion non-linearly, as shown in Fig. 13. In our model of cohesive particles [59], overlaps are always positive for both positive and negative

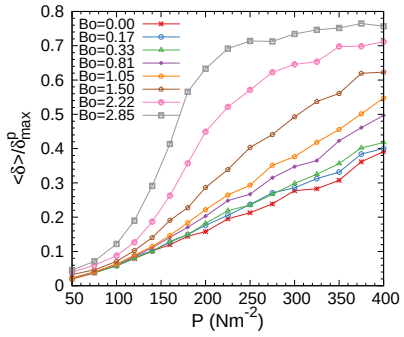


FIG. 13: (Color online) Normalized mean overlap $\frac{<\delta>}{\delta^p_{\max}}$ inside the shear band plotted against pressure, where different symbols represent the global Bond number (as given in the inset).

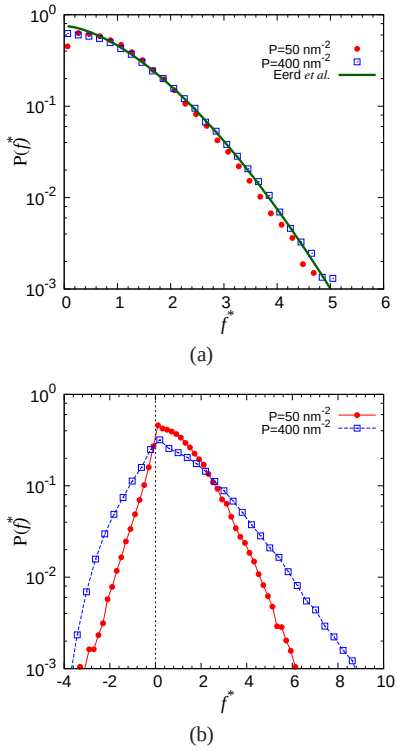


FIG. 14: (Color online) Probability distribution of the normalized force for (a) cohesion-less $Bo = 0$ and (b) highly cohesive $Bo = 2.85$ systems at different pressures in the system. Different symbols represent value of local pressure (as given in the inset).

forces. It is worth mentioning that for low *Bo*, the time evolution of $\langle\delta\rangle$ saturates quickly, while for $Bo = 1.5, 2.22, 2.85$ it takes longer to longer to reach the steady state due to the plastic increase of the overlap in average [53].

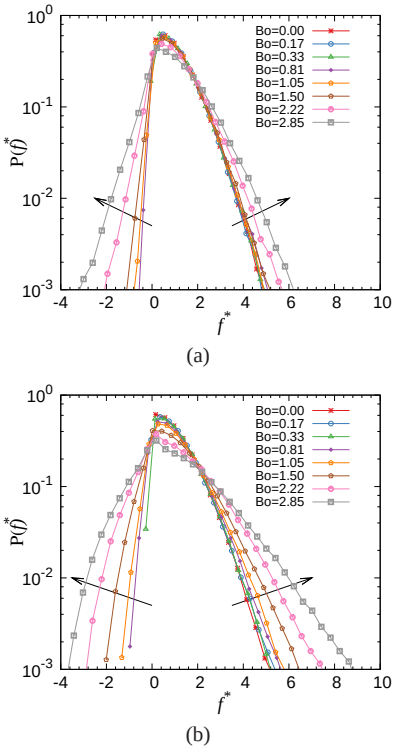


FIG. 15: (Color online) Probability distribution of normalized force $f^*$ for (a) low pressure $p = 50$ Nm$^{-2}$ (close to top) and (b) high pressure $p = 400$ Nm$^{-2}$ (close to bottom) in the system for data inside the shear band. Different symbols represent the global Bond number *Bo* (as given in the inset).

### 2. *PDFs of forces and structures of strong force chains in shear bands*

The probability distribution function (PDF) of forces are also strongly affected by cohesion. Figure 14 shows the PDFs of normal forces in shear bands for different pressure and cohesion, where the forces are scaled by the mean normal force, i.e. $f^* \equiv f/\langle f\rangle$. As can be seen, the PDF in the shear band for cohesion-less particles is almost independent of pressure (Fig. 14(a)), while it *depends on pressure* if the cohesive forces are very strong (Fig. 14(b)). Figure 15 displays the variations of the PDFs for different intensities of cohesion, where we find that the PDF becomes broad with increasing cohesion for $Bo > 1$. Therefore, *strong cohesion, which leads the system to a "mechanically frustrated state" induces larger fluctuations of positive/negative forces*. We note that Yang et al. [51] also found similar trends in static three-dimensional packings for small sized particles, where the PDF becomes broader, as particle size decreases, i.e. cohesion increases. Broadening of the PDFs was also observed by Luding et al. [75] during cooling down of a sintered system.

The cohesive forces change not only the shapes of the PDFs, but also their asymptotic behavior, i.e. the structure of strong force chains. At first, we fit their tails by a stretched

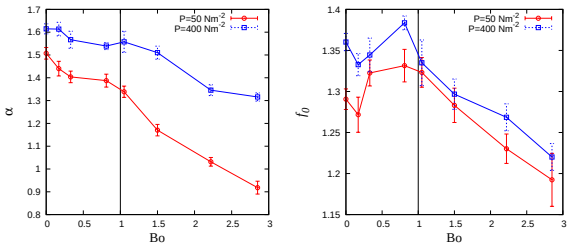


FIG. 16: (Color online) Fit parameters (a) $\alpha$ and (b) $f_0$ plotted against Bond number *Bo*. Different symbols represent value of local pressure (as given in the inset).

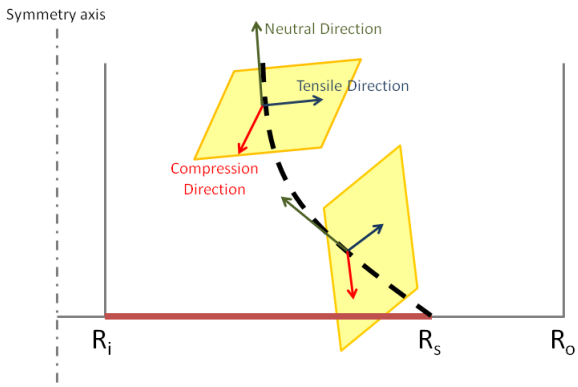


FIG. 17: (Color online) A sketch showing the shear band as dotted line, shear plane, and three eigen-directions of the strain rate tensor. Grey lines show inner and outer cylinders, while solid brown line shows the split, dashed black line shows the shear band which initiates at the split at bottom and moves towards inner cylinder as it moves towards the top. Green arrow represents the eigen-direction for neutral eigenvalue of the strain rate tensor, which is tangential to the shear band, perpendicular to this vector is the shear plane (yellow shaded region), which contains the eigen-directions for compression (red arrow) and tensile (blue arrow) eigenvalues.

exponential function [76]

$$P(f^*) \sim e^{-(f^*/f_0)^\alpha} \tag{9}$$

with a characteristic force $f_0$ and a fitting exponent $\alpha$. Figure 16 displays the characteristic force and the exponent against the global Bond number *Bo*. If $Bo < 1$, we obtain $f_0 = 1.4 \pm 0.1$ and $\alpha = 1.6 \pm 0.1$, which is very close to that predicted by Eerd et al. [76] for three-dimensional non-cohesive ensemble generated by MD simulations. For $Bo > 1$, however, both characteristic force and fitting exponent decrease with increasing cohesion. The decreasing fitting exponent hints at stronger fluctuations in the force distribution. A Gaussian tail of the probability distribution would indicate a more homogeneous random spatial distribution of forces. The deviation towards an exponential distribution can be linked to an increase in heterogeneity in the spatial force distribution; as mentioned in previous studies [77–79]. Therefore, we conclude that *the tail of the PDF becomes more exponential with increasing cohesion, which implies a heterogeneous spatial distributions of strong forces*.

Also we observe that the fitting exponent decreases with increasing pressure, which implies that at high pressure where cohesion is more active due to the contact model the spatial distribution is more heterogeneous compared to that for low pressure.

### C. Anisotropy of force chain networks in shear bands

In the case of simple shear, there are two non-zero eigenvalues of the strain rate tensor, which are equal in magnitude but opposite in sign, and the third eigenvalue is zero. The plane containing the eigen-vectors with non-zero eigenvalues is called the "shear plane", where the eigen-vector with zero eigenvalue is perpendicular to this plane (parallel to the shear band). We call the eigen-directions with positive, negative, and zero eigenvalues as the *compressive*, *tensile*, and *neutral* directions, respectively. Since the compressive and tensile directions are associated with loading and unloading of contacts, respectively, it is intuitive that in the absence of any external force, the mean force would be positive in compressive direction, negative in tensile direction, and almost zero in neutral direction.

In our system, both compressive forces and shear play a combined role, where the neutral direction gets a contribution from external compressive force only, while the two principal (compressive and tensile) directions get contributions from both shear and external compressive force. Because the cohesive force is activated by unloading, it should affect the force along the tensile direction. Note that the shear band here is not vertical, instead its orientation changes with depth as shown in the schematic in Fig. 17. In this figure, the eigen-direction of the neutral (zero) eigenvalue (green arrow) moves with the shear band. This turning of the neutral eigen-direction makes the shear plane tilt as well (which is shown by the yellow shaded regions). To extract the contacts aligned along these directions at a given pressure in the system, we first calculate the local strain rate tensor and extract the three eigen-directions $\mathbf{n}_\gamma$. Next, we look for contacts with unit contact vector $\mathbf{n}_c$, which satisfy the condition $|\mathbf{n}_c.\mathbf{n}_\gamma| \geq 0.9$ . The contacts which satisfy the condition for compressive eigen-direction are termed compressive, and tensile and neutral contacts are defined similarly. The forces carried by compressive, tensile, and neutral contacts are denoted by $f_{\rm com}$, $f_{\rm ten}$, and $f_{\rm neu}$ respectively.

Figure 18 shows the mean forces relative to overall local mean force, $f'_{\rm com/ten/neu} \equiv \langle f_{\rm com/ten/neu} \rangle - \langle f \rangle$, plotted against pressure for different values of *Bo*. We find that $f'_{\rm com}(>0)$ and $f'_{\rm ten}(<0)$ are symmetric about zero, and $f'_{\rm neu} \simeq 0$. Because the mean force along the neutral direction is independent of *Bo*, the cohesion does not affect the neutral direction (due to the absence of shear in this direction). However, $f'_{\rm ten}$

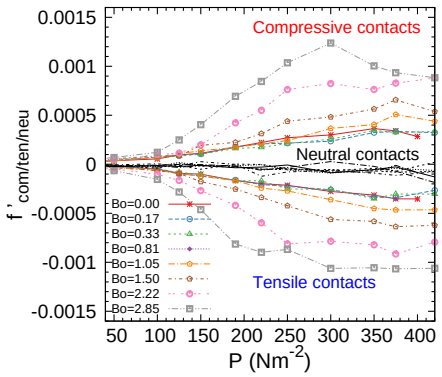


FIG. 18: (Color online) Mean forces in different eigen-directions of the strain rate tensor, relative to the overall mean force plotted against the local pressure in the system. Different symbols represent the global Bond number *Bo* (as given in the inset).

decreases with pressure and cohesion, while $f'_{\rm com}$ increases to keep the mean overall force to stay independent of cohesion. Both positive and negative forces are present in all directions. However, the positive and negative forces dominate in the compressive and tensile directions, respectively. *The anisotropy of forces is more pronounced with increasing pressure and cohesion*, as observed in Fig. 8.

Next, we study the PDFs of forces in the compressive, tensile, and neutral directions. Figure 19 displays the PDFs along each direction for non-cohesive $Bo = 0$ and highly cohesive $Bo = 2.85$ systems, where the forces along different directions are normalized by the overall mean force. In a non-cohesive system (Fig. 19(a)), we observe that for $f^* < 1$, the PDF along the tensile direction is higher compared to that for the compressive direction, which is intuitive as the majority of contacts will have smaller forces in the tensile direction. For $f^* > 1$, however, the PDF along the compressive direction is higher compared to that along the tensile direction, as force along the compressive direction should be stronger compared to that along the tensile direction [80]. For a highly cohesive system (Fig. 19(b)), a similar behavior is observed for positive forces, while for small positive and negative forces, due to attractive forces the probability is higher along the tensile direction compared to the compressive direction. The PDFs of forces in the neutral direction lie in between those in compressive and tensile directions, suggesting a close to average distribution of forces in the neutral direction.

Figure 20 shows the variations of the PDFs along compressive and tensile directions for different values of *Bo*. If $Bo < 1$, the PDFs collapse on top of each other. However, the PDFs get wider with increasing cohesion above $Bo = 1$ (such widening is more prominent for positive and negative forces in the compressive and tensile directions, respectively). Again, we confirm that strong cohesion leads to an increases of positive and negative forces in the compressive and tensile directions, respectively. Therefore, *the force distributions in the principal directions gets more heterogeneous with increasing cohesion for* $Bo > 1$, and hence the heterogeneity of the overall force

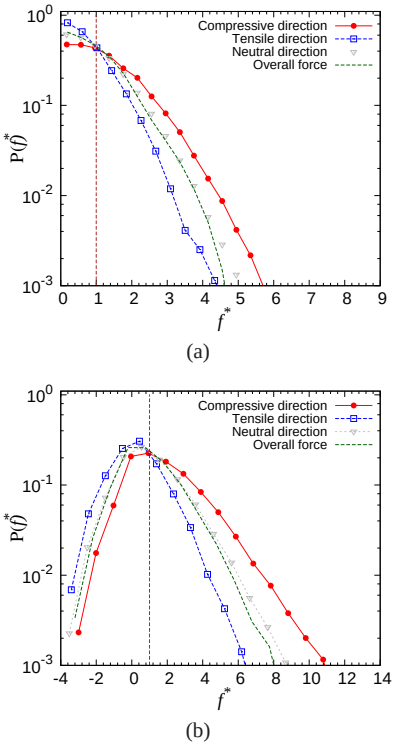


FIG. 19: (Color online) Probability distributions of normalized forces $f^* = f/\langle f\rangle$ in compressive, tensile, and neutral directions inside the shear bands. Here, we show the results for high pressure in (a) non-cohesive $Bo = 0$ and (b) high cohesive $Bo = 2.85$ systems. The PDFs of the overall normalized forces are shown as dashed line.

structure increases.

The results in this section, suggest that for low *Bo*, compressive forces and shear dominates and governs the distribution of forces along compressive and tensile directions. The forces respond to external compression and shear, i.e., due to shear, particles can rearrange and avoid very large forces. In contrast, for high *Bo*, cohesion dominates over external compression and the contact forces respond mainly to cohesion and shear. Due to the sticky nature of cohesive forces, rearrangements of the contact network become difficult, and very large contact forces as well as strong sticking forces occur together, and hence the contact network becomes more heterogeneous.

## IV. DISCUSSION AND CONCLUSION

In this paper, we have studied the effect of cohesion on shear banding in dry cohesive powders. We used a dimensionless parameter the global *Bond number Bo* to quantify how strong cohesive forces are relative to compressive forces. We found that $Bo \simeq 1$, very well predicts the transition from a free-flowing, non-cohesive system to a cohesive system. Interestingly, we found that also many other features of the system show a transition at $Bo \approx 1$.

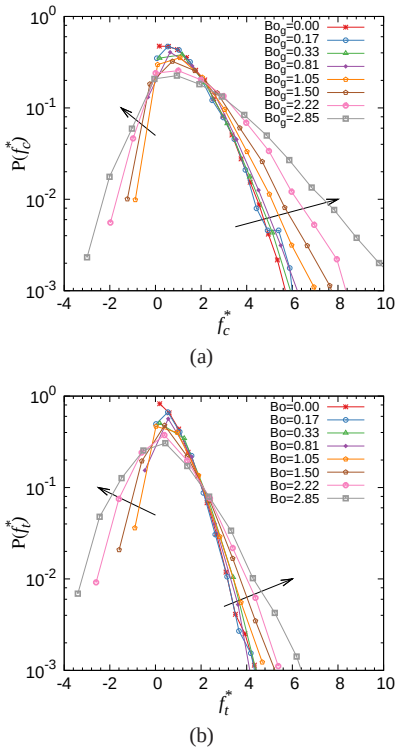


FIG. 20: (Color online) Probability distributions of normalized forces in (a) compressive ($f_c^* = f_c/\langle f\rangle$) and (b) tensile ($f_t^* = f_t/\langle f\rangle$) directions inside the shear bands. Here, we show the results for high pressure and different strength of cohesion, where different symbols represent the global Bond number *Bo* (as given in the inset).

*a. Shear band* Width and center position of the shear band for $Bo < 1$ stay fairly the same as for non-cohesive materials, and show a dependence on cohesion only for $Bo \geq 1$. Cohesive forces tend to keep the particles in contact to be connected, i.e., the cohesive forces assist the "collective motion" of particles. Thus the shear band, i.e., the velocity gradient, tends to be reduced. As a result, the width of the shear band increases with the strength of cohesion, i.e., the Bond number. This would imply that the presence of attractive forces works against the localization of shear.

*b. Forces and their direction dependence* The mean force $\langle f\rangle(P)$ (with $P \propto H - z$) is found to be independent of cohesion, like the number of contacts. With increasing *Bo*, stronger attractive negative forces are possible at the contact (which is intuitive). However, these negative forces must be balanced by some positive forces to maintain the same overall mean force. Therefore, the positive forces also must become larger as compared to non-cohesive systems.

Because we apply shear, compressive/tensile contact forces are induced in the system in compressive/tensile eigen–directions of the local strain rate tensor. However, there exists a direction along which no shear takes place. We observe that the mean force along this direction remains unaffected by cohesion, which implies that cohesive forces in the system are induced by shear. Both negative and positive forces are influenced along both tensile and compressive directions.

The mean force carried by contacts along compressive and tensile directions is *symmetric* about the mean overall force. For $Bo \leq 1$, this difference i.e. anisotropy of the force network is independent of cohesion, while for $Bo > 1$ the anisotropy in the force network increases with cohesion. Macroscopically, this anisotropy in force is directly related to the shear stress; the trend in force anisotropy is very similar to the trends found in the shear stress in previous work [53].

*c. Force probability distribution* Since granular systems are known to be heterogeneous in nature, we also analyzed the effect of cohesion on the force probability distributions. For non cohesive systems, no prominent effect of pressure on force distributions could be seen. For high cohesion $Bo > 1$, pressure affected the distribution of forces, by making the tails longer as compared to the case for $Bo \leq 1$. The distribution of forces showed that cohesion makes the force distribution *wide, and more symmetric*. Splitting up the force distributions along the compressive and tensile directions revealed that, for $Bo \leq 1$, the distributions are almost independent of cohesion. For higher *Bo*, cohesion broadens the force distributions along tensile direction, which in turn affects the distribution along the compressive direction. This suggests, an increase in heterogeneity in forces for $Bo > 1$ along compressive and tensile directions. For low *Bo*, the dynamics helps the particles to rearrange and avoid very strong forces. In contrast, for high *Bo*, cohesion induces stickiness at the contacts so that rearrangements are suppressed, increasing heterogeneity of the system, which is evident from longer tails of the probability distribution for system with higher *Bo*.

In conclusion, we have reported that both the flow profiles properties of the system (shear banding) and the force structure are unaffected by cohesion for $Bo \leq 1$. In contrast, for $Bo > 1$, cohesion strongly affects the flow, the anisotropy, and the internal force structure. Attractive forces have been found to reduce shear localization for $Bo > 1$. In the same regime, cohesion also promoted heterogeneity of the forces. These two observations independently are consistent with previous studies with attractive forces, concerning rheology [30] and force structures for static packings [51].

As speculation for a wider view, our results can be interpreted as follows: In the language of statistical mechanics, *Bo* corresponds to a "control parameter" and $Bo = 1$ to a "critical point". The critical changes in the characteristic force and the fitting exponent show a small pressure dependence, which could be better predicted using a pressure dependent local Bond number. Since the local *Bo* are close to the global *Bo*, the system can be classified by the latter. In our case, the macroscopic properties (position and width of shear-bands) and structural signatures (the tails of the PDFs) gradually increase from $Bo = 1$. This implies, that this increase, behaves like a "second-order transition". Confirming this would need a further detailed study. Also, experiments performed with controlled cohesive strength would be exciting to confirm and validate our results. Finally it would be interesting to reproduce our findings with different contact models, such as capillary bridges or even simpler linear contacts models.

### ACKNOWLEDGMENTS

We thank M. Wojtkowski, N. Kumar, O. I. Imole, and T. Weinhart for stimulating discussions. Financial support through the "Jamming and Rheology" project of the Stichting voor Fundamenteel Onderzoek der Materie (FOM), which is financially supported by the "Nederlandse Organisatie voor Wetenschappelijk Onderzoek" (NWO), is acknowledged.


### Appendix: Maximum attractive force

The extreme loading and unloading branches are reflected by the outer triangle in Fig. 1. Starting from a realized maximum overlap during loading, $\delta_{\max} < \delta^p_{\max}$, the unloading happens within the triangle, as can be characterized by a branch with stiffness

$$k_2 = k_1 + (k_p - k_1)\delta_{\max}/\delta^p_{\max} \tag{A.1}$$

(as given in [58]). The elastic, reversible force along this branch is given by $k_2(\delta - \delta_0)$ [58, 59]. The intermediate stiffness $k_2$ follows from a linear interpolation between $k_1$ and $k_p$, as explained in [58, 59]. The corresponding maximal attractive force is $f_{\rm m} = -k_c\delta_{\rm m} = -k_c\frac{(k_2-k_1)}{(k_2+k_c)}\delta_{\max}$. If we assume that the maximal overlap $\delta^p_{\max}$ is realized under a given external (compressive) pressure $p_{\max}$, then we can infer $\frac{p}{p_{\max}} = \frac{\delta_{\max}}{\delta^p_{\max}}$, with pressure $p$ being $p = k_1\delta_{\max}/A$, $A$ being a representative area. This leads to realized maximal attractive force being

$$f_{\rm m} = -k_c\frac{(k_2-k_1)}{(k_2+k_c)}\frac{p}{p_{\max}}\delta^p_{\max} \tag{A.2}$$

Using Eq. (A.1) in Eq. (A.2), we get

$$f_{\rm m} = -k_c\frac{(k_p-k_1)\frac{p_{\max}}{k_1}\left(\frac{p}{p_{\max}}\right)^2}{k_c+k_1+(k_p-k_1)\frac{p}{p_{\max}}}. \tag{A.3}$$

This definition can be used to define a local Bond number as $Bo^a_l(P) = f_{\rm m}(P)/\langle f(P)\rangle$, where mean force at that pressure is discussed in Sec. II C. This Bond number would be compared with various other definitions in Sec. II C.


[1] J. Bridgwater, Géotechnique **30**, 533 (1980).
[2] D. Howell, R. P. Behringer, and C. Veje, Phys. Rev. Lett. **82**, 5241 (1999).
[3] P. Schall and M. van Hecke, Ann. Rev. Fluid Mech. **42** (2010).
[4] G. Katgert, M. E. Möbius, and M. van Hecke, Phys. Rev. Lett. **101**, 058301 (2008).
[5] R. Höhler and S. Cohen-Addad, Journal of Physics: Condensed Matter **17**, R1041 (2005).
[6] G. Ovarlez, S. Rodts, X. Chateau, and P. Coussot, Rheologica Acta **48**, 831 (2009), ISSN 0035-4511.
[7] J. K. G. Dhont, M. P. Lettinga, Z. Dogic, T. A. J. Lenstra, H. Wang, S. Rathgeber, P. Carletto, L. Willner, H. Frielinghaus, and P. Lindner, Faraday Discuss. **123**, 157 (2003).
[8] G. Mandl, L. Jong, and A. Maltha, Rock Mech. **9**, 95 (1977), ISSN 0035-7448.
[9] J. P. Bardet and J. Proubet, Géotechnique **41**, 599 (1991).
[10] M. Oda and H. Kazama, Géotechnique **48**, 465 (1998).
[11] D. R. Scott, Nature **381**, 592 (1996).
[12] H.-B. Mühlhaus and I. Vardoulakis, Géotechnique **3**, 271 (1987).
[13] M. Lätzel, S. Luding, and H. J. Herrmann, Granular Matter **2**, 123 (2000).
[14] M. Lätzel, S. Luding, H. J. Herrmann, D. W. Howell, and R. P. Behringer, Eur. Phys. J. E **11**, 325 (2003).
[15] D. Fenistein and M. van Hecke, Nature **425**, 256 (2003).
[16] S. McNamara and W. R. Young, Phys. Rev. E **53**, 5089 (1996).
[17] S. McNamara and W. R. Young, Phys. Rev. E **50**, R28 (1994).
[18] K. Kamrin and G. Koval, Phys. Rev. Lett. **108**, 178301 (2012).
[19] D. L. Henann and K. Kamrin, P. N. A. S.(2013).
[20] M. A. S. Quintanilla, A. Castellanos, and J. M. Valverde, PAMM **3**, 206 (2003).
[21] J. M. Valverde, M. A. S. Quintanilla, and A. Castellanos, Phys. Rev. Lett. **92**, 258303 (2004).
[22] A. Castellanos, Advances in Physics **54**, 263 (2005).
[23] S. Herminghaus, Advances in Physics **54**, 221 (2005).
[24] C. Miclea, C. Tanasoiu, C. Miclea, F. Sima, M. Cioangher, and A. Gheorghiu, in *Powders and Grains 2005* (Balkema, 2005).
[25] L. Brendel, J. Török, R. Kirsch, and U. Brckel, Granular Matter **13**, 777 (2011), ISSN 1434-5021.
[26] A. Hatzes, F. Bridges, D. Lin, and S. Sachtjen, Icarus **89**, 113 (1991).
[27] F. Spaepen, Acta Meta. **25**, 407 (1977).
[28] J. Li, F. Spaepen, and T. C. Hufnagel, Philos. Mag. A **82**, 2623 (2002).
[29] L. Bécu, S. Manneville, and A. Colin, Phys. Rev. Lett. **96**, 138302 (2006).
[30] P. Chaudhuri, L. Berthier, and L. Bocquet, Phys. Rev. E **85**, 021503 (2012).
[31] J. Vermant, Current opinion in colloid & interface science **6**, 489 (2001).
[32] R. Höhler and S. Cohen-Addad, Journal of Physics: Condensed Matter **17**, R1041 (2005).
[33] P. Coussot and G. Ovarlez, The European Physical Journal E **33**, 183 (2010).
[34] N. Estrada, A. Lizcano, and A. Taboada, Phys. Rev. E **82**, 011303 (2010).
[35] R. Mani, D. Kadau, D. Or, and H. J. Herrmann, Phys. Rev. Lett. **109**, 248001 (2012).
[36] R. Schwarze, A. Gladkyy, F. Uhlig, and S. Luding, Granular Matter **15** (2013), ISSN 1434-5021.
[37] J. Yuan, Q. Zhang, B. Li, and X. Zhao, Bulletin of Engineering Geology and the Environment **72**, 107 (2013), ISSN 1435-9529.
[38] C. H. Liu, S. R. Nagel, D. A. Schecter, S. N. Coppersmith, S. Majumdar, O. Narayan, and T. A. Witten, Science **269**, 513 (1995).
[39] D. M. Mueth, H. M. Jaeger, and S. R. Nagel, Phys. Rev. E. **57**, 3164 (1998).

[40] G. Løvoll, K. J. Måløy, and E. G. Flekkøy, Phys. Rev. E **60**, 5872 (1999).
[41] D. L. Blair, N. W. Mueggenburg, A. H. Marshall, H. M. Jaeger, and S. R. Nagel, Phys. Rev. E **63**, 041304 (2001), cond-mat/0009313.
[42] T. S. Majmudar and R. P. Behringer, Nature **435**, 1079 (2005).
[43] K. Liffman, D. Y. C. Chan, and B. D. Hughes, Powder Technol. **72**, 255 (1992).
[44] F. Radjai, D. E. Wolf, M. Jean, and J.-J. Moreau, Phys. Rev. Lett. **80**, 61 (1998).
[45] L. E. Silbert, G. S. Grest, and J. W. Landry, Phys. Rev. E **66**, 061303 (2002).
[46] J. H. Snoeijer, M. van Hecke, E. Somfai, and W. van Saarloos, Phys. Rev. E **67**, 030302 (2003).
[47] L. E. Silbert, Soft Matter **6**, 2918 (2010).
[48] V. Trappe, V. Prasad, L. Cipelletti, P. N. Segre, and D. A. Weitz, Nature **411**, 772 (2001).
[49] V. Richefeu, M. S. E. Youssoufi, and F. Radjaï, Phys. Rev. E **73**, 051304 (2006).
[50] F. A. Gilabert, J.-N. Roux, and A. Castellanos, Phys. Rev. E **75**, 011303 (2007).
[51] R. Y. Yang, R. P. Zou, A. B. Yu, and S. K. Choi, Phys. Rev. E **78**, 031302 (2008).
[52] F. Radjai, V. Topin, V. Richefeu, C. Voivret, J. Delenne, E. Azéma, and S. El Youssoufi, AIP Conf. Proc. **1227**, 240 (2010).
[53] S. Luding and F. Alonso-Marroquín, Granular Matter **13**, 109 (2011).
[54] S. T. Nase, W. L. Vargas, A. A. Abatan, and J. McCarthy, Powder Technol. **116**, 214 (2001).
[55] P. G. Rognon, J. Roux, and M. Naaím, J. of Fluid Mech. **596**, 21 (2008).
[56] M. P. Allen and D. J. Tildesley, *Computer Simulation of Liquids* (Oxford University Press, 1987).
[57] P. A. Cundall, in *Proc. Symp. Int. Rock Mech.*, Vol. 2 (Nancy, 1971).
[58] A. Singh, V. Magnanimo, and S. Luding, AIP Conf. Proc. **1542**, 682 (2013).
[59] S. Luding, Granular Matter **10**, 235 (2008).
[60] J. Tomas, Granular Matter **6**, 75 (2004).
[61] C. Thornton and Z. Ning, Powder Technology **12** (1998).
[62] S. C. Thakur, H. Ahmadian, J. Sun, and J. Y. Ooi, Particuology(2013).
[63] M. Pasha, S. Dogbe, C. Hare, A. Hassanpour, and M. Ghadiri, Granular Matter **16**, 151 (2014).
[64] D. Fenistein, J. W. van de Meent, and M. van Hecke, Phys. Rev. Lett. **92**, 094301 (2004).
[65] S. Luding, Particulate Science and Technology **26**, 33 (2008).
[66] S. Luding, Particuology **6**, 501 (2008).
[67] J. A. Dijksman and M. van Hecke, Soft Matter **6**, 2901 (2010).
[68] T. Unger, J. Török, J. Kertész, and D. E. Wolf, Phys. Rev. Lett. **92**, 214301 (2004).
[69] D. Fenistein, J.-W. van de Meent, and M. van Hecke, Phys. Rev. Lett. **96**, 118001 (2006).
[70] A. Ries, D. E. Wolf, and T. Unger, Phys. Rev. E **76**, 051301 (2007).
[71] F. da Cruz, S. Emam, M. Prochnow, J.-N. Roux, and F. Chevoir, Phys. Rev. E **72**, 021309 (2005).
[72] G. Ovarlez, S. Rodts, A. Ragouilliaux, P. Coussot, J. Goyon, and A. Colin, Phys. Rev. E **78**, 036307 (2008).
[73] X. Wang, H. P. Zhu, S. Luding, and A. B. Yu, Phys. Rev. E **88**, 032203 (2013).
[74] M. R. Shaebani, M. Madadi, S. Luding, and D. E. Wolf, Phys. Rev. E **85**, 011301 (2012).
[75] S. Luding, K. Manetsberger, and J. Müllers, Jour. Mech. and Phys. Solids **53**, 455 (2005), `http://www.sciencedirect.com/science/article/pii/S00225`
[76] A. R. T. van Eerd, W. G. Ellenbroek, M. van Hecke, J. H. Snoeijer, and T. J. H. Vlugt, Phys. Rev. E **75**, 060302 (2007).
[77] F. Radjai, M. Jean, J.-J. Moreau, and S. Roux, Phys. Rev. Lett. **77**, 274 (1996).
[78] H. A. Makse, D. L. Johnson, and L. M. Schwartz, Physical review letters **84**, 4160 (2000).
[79] H. Zhang and H. Makse, Physical Review E **72**, 011301 (2005).
[80] B. P. Tighe, J. E. S. Socolar, D. G. Schaeffer, W. G. Mitchener, and M. L. Huber, Phys. Rev. E **72**, 031306 (2005).